

Published in final edited form as:

Magn Reson Med. 2014 July ; 72(1): 149–159. doi:10.1002/mrm.24918.

Quantitative Oxygenation Venography from MRI Phase

Audrey P. Fan^{1,2,*}, Berkin Bilgic^{1,2}, Louis Gagnon^{2,3}, Thomas Witzel², Himanshu Bhat⁴, Bruce R. Rosen^{2,3}, and Elfar Adalsteinsson^{1,2,3}

¹Magnetic Resonance Imaging Group, Research Laboratory of Electronics, Department of Electrical Engineering and Computer Science, Massachusetts Institute of Technology, Cambridge, Massachusetts, USA

²Athinoula A. Martinos Center for Biomedical Imaging, Department of Radiology, Massachusetts General Hospital, Charlestown, Massachusetts, USA

³Harvard-MIT Health Sciences and Technology, Cambridge, Massachusetts, USA

⁴Siemens Medical Solutions USA Inc., Charlestown, Massachusetts, USA

Abstract

Purpose—To demonstrate acquisition and processing methods for quantitative oxygenation venograms that map in vivo oxygen saturation (SvO₂) along cerebral venous vasculature.

Methods—Regularized quantitative susceptibility mapping (QSM) is used to reconstruct susceptibility values and estimate SvO₂ in veins. QSM with ℓ_1 and ℓ_2 regularization are compared in numerical simulations of vessel structures with known magnetic susceptibility. Dual-echo, flow-compensated phase images are collected in three healthy volunteers to create QSM images. Bright veins in the susceptibility maps are vectorized and used to form a three-dimensional vascular mesh, or venogram, along which to display SvO₂ values from QSM.

Results—Quantitative oxygenation venograms that map SvO₂ along brain vessels of arbitrary orientation and geometry are shown in vivo. SvO₂ values in major cerebral veins lie within the normal physiological range reported by ¹⁵O positron emission tomography. SvO₂ from QSM is consistent with previous MR susceptometry methods for vessel segments oriented parallel to the main magnetic field. In vessel simulations, ℓ_1 regularization results in less than 10% SvO₂ absolute error across all vessel tilt orientations and provides more accurate SvO₂ estimation than ℓ_2 regularization.

Conclusion—The proposed analysis of susceptibility images enables reliable mapping of quantitative SvO₂ along venograms and may facilitate clinical use of venous oxygenation imaging.

Keywords

venous oxygen saturation; quantitative susceptibility; brain oxygenation; venography

INTRODUCTION

Continuous oxygen delivery to neural tissue is necessary to maintain normal brain function and viability. Noninvasive imaging of brain oxygenation would provide new metabolic biomarkers to study cerebral physiology at rest and during functional activity (1,2). Oxygenation imaging can also improve understanding of disorders in which oxygen supply to the brain is disturbed, such as stroke (3–5), tumor (6,7), and multiple sclerosis (8,9). In acute stroke, for instance, metabolic indicators such as local oxygen extraction have been shown to identify tissue at risk of infarction and guide treatment of the disease (4).

Gradient echo MRI can be used to quantify venous oxygen saturation (SvO_2) in individual veins from the magnetic susceptibility shift between vessels and brain tissue. This susceptibility shift is modulated by the presence of paramagnetic deoxyhemoglobin molecules, and through the blood hematocrit relates to the oxygenation level of the vein (10). Previous MRI studies have modeled cerebral veins as long cylinders to quantify blood oxygenation from T_2^* signal decay profiles internal and external to the vessel (11–13), as well as from phase signal differences between the vein and tissue (10,14). Advantages of the phase-based approach, known as MR susceptometry, include use of gradient echo acquisitions that are readily available on most scanners and self-calibration to absolute SvO_2 by means of reference phase values in cerebral tissue.

Recently, MR susceptometry has been applied to study oxygenation in large draining veins of the brain (14,15) and locally in smaller pial vessels (16,17) that are parallel to the main field (B_0). In addition, susceptibility-based SvO_2 has been combined with MRI flow measurements from arterial spin labeling (16) and phase-contrast imaging (15,18) to assess the cerebral metabolic rate of oxygen consumption. Other studies have also considered the effect of vessel tilt angle and cross-section on oxygenation estimates (19,20). Although these simulations revealed good SvO_2 agreement with expected values in near-parallel veins after correction for vessel tilt, nearly 40% absolute SvO_2 error was found for tilt angles of 50° or greater relative to B_0 (20). As a result, clinical application of phase-based SvO_2 imaging is currently restricted to vessel segments within a limited range of orientations that prevents use of the technique across the brain.

To address these limitations, we propose to measure oxygenation directly on quantitative susceptibility mapping (QSM) images reconstructed from MRI phase images. From QSM, susceptibility values are available along any vein without cylinder orientation assumptions, enabling SvO_2 estimation in a larger set of vessels. Susceptibility mapping has been developed to assess iron deposition (21,22), probe the anisotropic structure of white matter tracts in the brain (23), and characterize cerebral pathology including lesions (24) and microbleeds (25). QSM reconstruction is challenging because k-space information of the observed field map is innately undersampled or damped due to nulls and small values in the dipole kernel near the magic angle (54.7°) (26,27), such that recovery of the underlying susceptibility is ill-posed. Current QSM approaches condition the inversion problem of estimating magnetic susceptibility from MRI phase by k-space thresholding of large values in the deconvolution kernel near the magic angle (28,29); collecting multiple sets of phase data where the subject is placed in different physical positions between scans (22,30); or

applying mathematical regularization through use of priors on the expected susceptibility distribution (21,31–33). These QSM methods present different artifact and noise properties (34), and careful selection of QSM reconstruction settings is necessary for accurate SvO₂ measurements.

In this work, we propose a new method to analyze and visualize susceptibility maps for robust SvO₂ estimation in veins across the brain. The reconstruction process combines QSM with vascular graphing routines originally developed for high-resolution optical imaging of microvasculature (35). Cerebral veins in QSM maps are vectorized into a representation of nodes and edges, such that SvO₂ values can be averaged along physiological vessel segments for increased signal-to-noise (SNR). Importantly, the graph structure also allows for evaluation of the fidelity of oxygenation measurements across various tilt angle orientations of cerebral veins in vivo. Through this approach, quantitative oxygenation venograms that map SvO₂ along each vessel are shown in healthy volunteers at 3 Tesla (T).

METHODS

Relationship Between SvO₂ and Magnetic Susceptibility

The proposed method estimates SvO₂ from magnetic susceptibility measurements in venous blood. The susceptibility shift between venous blood and water ($\chi_{\text{vein-water}}$) is dominated by the oxygenation-dependent concentration of paramagnetic deoxyhemoglobin molecules in blood. This susceptibility difference is related to SvO₂ in the vessel as (10):

$$\Delta\chi_{\text{vein-water}} = (1 - \text{SvO}_2) \cdot \Delta\chi_{\text{do}} \cdot \text{Hct} + \Delta\chi_{\text{oxy-water}} \cdot \text{Hct} \quad [1]$$

where hematocrit (*Hct*) is the percent of blood that consists of erythrocytes, χ_{do} is the susceptibility shift per unit hematocrit between fully oxygenated and fully deoxygenated erythrocytes, and $\chi_{\text{oxy-water}}$ is the susceptibility shift between oxygenated blood cells and water.

Here χ_{do} is assumed to be 0.27 ppm (cgs) for calibration of SvO₂ values, as previously done for femoral veins (19) and large, draining brain vessels (15). The value was first reported by Spees et al (36) and was recently corroborated in an independent MRI study (37). However, this assumed χ_{do} is different from earlier reported values of 0.2 ppm (38,39) and 0.18 ppm (10), which have also been used to calibrate SvO₂ measurements (14,17). The current study adopts $\chi_{\text{do}} = 0.27$ ppm from the more recent studies, which address several potential sources of measurement error in earlier work, such as erythrocyte settling within stationary samples. It is noted that use of the earlier value $\chi_{\text{do}} = 0.18$ ppm leads to lower SvO₂ estimates by ~13% absolute oxygenation (16). In contrast, oxygenated blood exhibits a much smaller diamagnetic shift of $\chi_{\text{oxy-water}} = -0.03$ ppm (10), and given a physiological *Hct* of 40% (40), the susceptibility contribution of oxygenated erythrocytes (-0.01 ppm) is small compared with the paramagnetic shift driven by deoxyhemoglobin.

As magnetic susceptibility measurements are intrinsically relative, reproducible quantification of SvO₂ from blood susceptibility requires a reference with respect to a standard tissue region. In previous work, venous susceptibility has been referenced to

neighboring brain tissue (16,17). However, this approach does not account for regional variations in tissue susceptibility between gray and white matter (41) or increased susceptibility in ironrich structures of the basal ganglia (21). In this study, blood susceptibility is instead referenced to cerebrospinal fluid (CSF), by assigning 0ppm to the mean susceptibility of the anterior portion of the ventricles (42,43). Care was taken to avoid voxels near paramagnetic choroid plexus structures that could distort reference susceptibility values (44).

Although susceptibility imaging can provide physiological information about oxygen saturation in veins, there is no MRI contrast mechanism to directly measure susceptibility. Instead, the underlying susceptibility distribution (χ) of the brain, if placed in a strong magnet, induces field perturbations through a complex and nonlocal relationship (26). In practice, MRI is sensitive to the resulting field distribution (b), which manifests on gradient echo phase images as $\phi = \gamma \cdot b \cdot TE$. Here, γ is the proton gyromagnetic ratio and TE is the echo time.

To simplify the estimation of susceptibility from phase for the purpose of SvO₂ measurements, MR susceptometry studies have modeled vessel segments as infinite cylinders. For veins approximated as long cylinders approximately parallel to B₀, a simple analytical relationship exists between the local field and blood susceptibility in the vein:

$$\Delta b_{vein-water} = \frac{1}{6} \cdot 4\pi \cdot \Delta\chi_{vein-water} \cdot (3\cos^2\theta_{vein} - 1) \cdot B_0 \quad [2]$$

where θ_{vein} denotes the vein tilt angle relative to B₀. The majority of MR susceptometry literature investigates oxygenation in veins parallel to the main field (14–17), although a few have also considered perpendicular geometries (12,13).

Regularized Approaches for Quantitative Susceptibility Mapping

As an alternative, this work proposes to measure SvO₂ through reconstruction of three-dimensional (3D) quantitative susceptibility maps, from which blood susceptibility and oxygenation level can be directly read along cerebral veins. Instead of applying a cylinder model for cerebral vessels, the new method makes prior assumptions about spatial variations in the underlying susceptibility distribution. Regularization is a mathematical technique to incorporate such prior information to solve an ill-posed problem, and several regularized approaches have been explored to reconstruct susceptibility maps from single-orientation field maps (21,32,33,45).

In this work, the regularization terms impose prior beliefs on the spatial gradients of susceptibility. For instance, the ℓ_1 -norm penalty term promotes a sparse number of nonzero spatial gradients in χ , such that the optimal χ is favored to be piecewise constant within anatomical tissue boundaries. The ℓ_1 -regularized optimization problem is:

$$\chi^* = \underset{\chi}{\operatorname{argmin}} \|b - F^{-1}DF\chi\|_2^2 + \lambda_1 \cdot \|G\chi\|_1 \quad [3]$$

where $|y|_2 = \sqrt{y^T y}$ and $|y|_1 = \sum y_i$. Here $G = [G_x \ G_y \ G_z]^T$ is the gradient operator and λ_1 is a weighting parameter that trades off between data consistency (first term) and imposed spatial prior (second term). The *argmin* notation stands for argument of the minimum, i.e., the optimal susceptibility distribution which minimizes the value of the expression.

In contrast, the ℓ_2 -norm penalty promotes a slowly varying, smooth χ solution with a large number of small gradient coefficients. The ℓ_2 -regularized method solves the following optimization problem:

$$\chi^* = \operatorname{argmin}_{\chi} \|b - F^{-1}DF\chi\|_2^2 + \lambda_2 \cdot \|G\chi\|_2^2. \quad [4]$$

This study compares ℓ_1 and ℓ_2 regularization in the context of quantifying susceptibility shifts within narrow vessel structures.

Numerical Simulations

To assess the fidelity of SvO₂ measurements from QSM, numerical phantoms were generated with known susceptibility values in vessels. The susceptibility phantoms were simulated with matrix size = 240 × 240 × 154; spatial resolution = 1 × 1 × 1 mm³; brain anatomy based on the SRI24 brain atlas (46); and susceptibility values of −8.995, −9.045, and −9.04 ppm, respectively, for gray matter, white matter, and CSF (41). To minimize phase wrapping due to bulk susceptibility interfaces, voxels outside of the brain were assigned susceptibility values identical to gray matter. Veins were approximated as cylinders with 2-mm radius and length-to-radius ratio of 20, with susceptibility values corresponding to SvO₂ = 65% and Hct = 40%.

Local field maps were simulated from the constructed susceptibility distributions through multiplication with the dipole kernel in k-space (26). To avoid aliasing, each susceptibility map was padded to 480 × 480 × 308 matrix size with gray matter values before convolution. Phase images were then simulated from the field maps for TE = 20 ms and field strength of 3T, while the associated magnitude signal was assumed to be uniform across the brain. Gaussian noise was added to the real and imaginary part of the complex signal to achieve SNR of 35.6, which was the mean SNR observed across the brain in a healthy subject at TE = 20 ms. We note that in practice, venous blood signal experiences faster T₂* decay (~25 ms) relative to the surrounding brain tissue (~56 ms) such that SNR levels would not be spatially uniform as in the simulations. After addition of noise, the phase images were rescaled into field maps that served as the numerical input into the QSM algorithm.

Initial simulations with a parallel vessel compared ℓ_1 - and ℓ_2 -regularized QSM for 46 regularization parameters, chosen logarithmically between 10^{−6} and 10². The optimal weightings λ_1 and λ_2 were selected by the discrepancy principle. The discrepancy principle is a heuristic approach that identifies the optimal λ for which the squared residual of the data consistency term in the optimization (Eqs. [3] and [4]) matches the noise variance of the data (47). Finally, numerical simulations were repeated for vessel tilt angles ranging from 0–90° relative to B₀, in intervals of 5°, through modifying the vessel model in object space while maintaining the same vein length and susceptibility values.

MRI Acquisition

Experiments were performed on a Siemens 3T MAGNETOM Trio a Tim System with a 32-channel receive head coil. Three healthy volunteers (two female and one male, ages 25–26 years) were scanned with written consent under the local Institutional Review Board.

We implemented a dual-echo gradient echo sequence with flow compensation along all spatial axes at each echo (48). High-resolution gradient echo scans were acquired: repetition time (TR) = 26 ms; TE = 8.1, 20.3 ms; matrix size = $384 \times 336 \times 224$; resolution = $0.6 \times 0.6 \times 0.6 \text{ mm}^3$; flip angle = 15° ; bandwidth (BW) = 260 Hz/pixel; GRAPPA acceleration factor = 2; phase partial Fourier = 75%; acquisition time (TA) = 15:42 min. Separate low-resolution, single-echo gradient echo scans were also collected with the same spatial coverage: TR = 15 ms; TE = 6–10 ms spaced by 1 ms; matrix size = $128 \times 112 \times 56$; resolution = $1.8 \times 1.8 \times 2.4 \text{ mm}^3$; FA = 15° ; BW = 260 Hz/pixel; TA = 1:20 min per echo. No shimming was performed between the scans, and uncombined magnitude and phase images were saved for all acquisitions.

Quantitative Susceptibility Map Reconstruction

The RF phase offset map corresponding to TE = 0 was estimated separately for each receive channel from the five acquired echoes at the lower resolution (49). The estimated offset maps were subtracted from each receive channel of the 0.6-mm resolution data before coil combination with weighted averaging (50). This process was performed independently to generate 0.6-mm isotropic resolution phase images, φ_{TE1} and φ_{TE2} , at TE = 8.1 and 20.3 ms respectively.

After coil combination, φ_{TE1} and φ_{TE2} were unwrapped by means of FSL Prelude in 3D (51) with use of brain mask defined from the magnitude images by the FSL Brain Extraction Tool (52). Unreliable voxels with nonlinear phase evolution across echo times were identified as high spatial frequency structures on the phase offset map $\varphi_{0,\text{hires}} = \varphi_{\text{TE1}} - (\varphi_{\text{TE2}} - \varphi_{\text{TE1}}) \text{TE}_1 / (\text{TE}_2 - \text{TE}_1)$ (22). A voxel was considered unreliable if $|\varphi_{0,\text{hires}} - \varphi_{0,\text{smooth}}|$ exceeded $\pi/4$ radians, where $\varphi_{0,\text{smooth}}$ represents a fourth-order polynomial fit to the high-resolution $\varphi_{0,\text{hires}}$ map. The corrupt voxels constituted 2.1% of total brain voxels on average and were removed from the brain mask for all subsequent processing.

For each volunteer, a field map estimate was calculated as $b = \varphi_{\text{TE2}} / (\gamma \cdot \text{TE}_2 \cdot B_0)$. Background field contributions were estimated by 100 iterations of the projection onto dipole fields (PDF) routine (53) for removal, resulting in a local field map as input into the QSM algorithm. The optimal λ parameters were determined in one subject by means of the discrepancy principle, based on the noise variance $\sigma_{\text{scaled}}^2 = [\sigma / (A \cdot \gamma \cdot B_0 \cdot \text{TE} \cdot 10^{-6})]^2$ where σ^2 is the underlying standard deviation of noise estimated from the complex signal at TE = 20.3 ms; and A is the mean magnitude intensity across the brain for the subject. Only the ℓ_1 -regularized susceptibility maps were further processed to create venograms, and the same optimal λ_1 weighting was used across all volunteer datasets. CSF susceptibility was averaged for each volunteer from manually drawn regions of interest (ROIs) (mean volume = $4.8 \pm 1 \text{ cm}^3$), and subtracted from the QSM map.

Vessel Graphing and Display of Quantitative SvO₂ Venograms

Each in vivo susceptibility map was thresholded at $\chi > 0.15$ ppm to preserve venous structures with relatively high susceptibility values. The Volumetric Image Data Analysis (VIDA) software, originally developed to vectorize 3D vascular volumes from optical imaging for quantitative analysis, was adapted to graph vessels in the thresholded χ maps (35). The output of VIDA is a graph representation of the venous vasculature as nodes (placed inside the vessels) and edges (between the nodes to indicate connected vessel segments). Vessel diameter was automatically estimated at each node as described in (54). Manual editing was performed to adjust node positions that did not accurately align with vasculature, and to adjust vessel diameter for larger veins if underestimated by the automated procedure.

The graphed output was then rendered into a volumetric mesh, or venogram, which displays the venous vasculature in 3D with appropriate thickness (55). Cylindrical ROIs were created around each vessel edge based on the edge diameter. To minimize partial volume effects, χ_{vein} was estimated for each vessel edge based on the maximum value of the corresponding cylindrical ROI. All oxygenation values made in vivo assumed Hct = 40% and $\chi_{\text{do}} = 0.27$ ppm. For increased SNR, SvO₂ values were averaged along each connected vein segment.

RESULTS

Effect of ℓ_1 versus ℓ_2 Regularization on SvO₂

In numerical simulation, the optimal regularization weightings determined by the discrepancy principle was $\lambda_1 = 3.0 \cdot 10^{-4}$ and $\lambda_2 = 1.5 \cdot 10^{-2}$ for ℓ_1 - and ℓ_2 -regularized QSM, respectively. Figure 1 illustrates the simulated vessel on reconstructed susceptibility maps for the under-regularized (λ smaller than optimum), optimally regularized, and over-regularized (λ larger than optimum) solutions. Figure 2 displays absolute error in SvO₂ values directly reconstructed from the QSM maps against various λ . Note that both QSM algorithms show similar profiles in Figure 2, with largest SvO₂ error corresponding to large λ . At the optimal regularization weighting, ℓ_1 -based QSM resulted in 1.6% absolute SvO₂ error relative to the true value of 65% in the vein; while ℓ_2 -based QSM resulted in 6.9% absolute SvO₂ overestimate due to underestimation of χ . This finding is consistent with literature reports of susceptibility underestimation with ℓ_2 -regularized QSM algorithms (34).

Similar in vivo values for $\lambda_1 = 4.5 \cdot 10^{-4}$ and $\lambda_2 = 1.0 \cdot 10^{-2}$ were identified from the first volunteer. A sagittal slice from the corresponding ℓ_1 - and ℓ_2 -regularized QSM maps is depicted in Figure 3. This slice contains a cortical pial vein, for which SvO₂ values were directly estimated $\chi_{\text{vein-CSF}}$. As in the numerical phantom, ℓ_1 -regularized QSM provided a lower SvO₂ of 66.5% in this vein compared with SvO₂ of 70.3% estimated by ℓ_2 -regularized QSM. Based on these initial experiences, further venogram processing was performed on ℓ_1 -regularized instead of ℓ_2 -regularized QSM images to avoid potential SvO₂ overestimation as observed in the phantom.

Comparison Between SvO₂ from MR Susceptometry and QSM

SvO₂ values were measured directly on susceptibility maps and compared with SvO₂ values from model-based MR susceptometry. The SvO₂ comparisons were made on 10 parallel vessel segments manually identified from an in vivo dataset acquired at TE = 20.3 ms. Vessels included in the analysis were visible in at least three consecutive axial slices and were viewed in the sagittal and coronal slices to confirm their orientation relative to B₀. The same ROIs identified in each vessel and in CSF were used for all measurements.

The phase volume was processed using homodyne filtering on a slice-by-slice basis (56). The Hanning filter widths were calculated to be 96/512, 64/512, and 32/512 of the image matrix size to match typical SWI processing parameters. Figure 4a–c displays the axial phase images after filtering and highlights a sample parallel vein used in the analysis. Phase measurements from the filtered images were modeled with a parallel cylinder to estimate SvO₂ (Eq. [2]). The mean SvO₂ values corresponding to different filter widths were statistically different, with *P* values significant at the 1% level after Bonferroni adjustment for multiple comparisons (Fig. 5).

Additional oxygenation measurements were made through application of MR susceptometry (Eq. [3]) on the local field map after PDF removal of global fields. The mean SvO₂ value across vessels modeled from the local field map (65.8% ± 4%) was not statistically different from the mean SvO₂ value directly measured from the QSM map (66.1% ± 5%) at the 5% significance level (*P* = 0.91, paired t-test with correction for multiple comparisons). The variance of SvO₂ estimates were also not different across the phase, fieldmap, and QSM techniques (*P* = 0.63 by Bartlett's test for equal variances). Furthermore, χ_{water} estimates from ventricle ROIs in the QSM maps were stable across subjects (mean values of 0.001 ± 0.05, 0.003 ± 0.04, and 0.016 ± 0.05 ppm, respectively), without large filter-dependent variations in CSF values observed in SWI homodyne filtering.

SvO₂ Reconstruction Profile Across Vessel Tilt Angle

SvO₂ estimated from ℓ_1 - and ℓ_2 -regularized QSM is plotted across vein tilt angles for numerical simulations (Fig. 6a,b). Both algorithms resulted in similar SvO₂ profiles over tilt angle, with maximum SvO₂ overestimate at approximately 45° relative to the main field. For all vessel orientations, ℓ_2 -regularized QSM resulted in greater overestimation of mean SvO₂ relative to ℓ_1 -regularized QSM (*P* < 10⁻⁴, paired t-test for each tilt angle). The error in mean SvO₂ measured by the ℓ_1 -based algorithm was less than 10% absolute oxygenation for all vessel tilt angles. For 15/18 of the investigated vessel orientations, ℓ_2 -regularized QSM exhibited greater SvO₂ variance relative to ℓ_1 -regularized QSM (*P* < 0.05, *F*-test for variance equality).

Quantitative Oxygenation Venograms In Vivo

Brain vessels were graphed from thresholded QSM maps in each volunteer with default VIDA parameters, including rod filter half-size of five voxels (Fig. 7). Across all subjects, the venous vasculature was represented on average by 1032 ± 70 edges inside the vessels. The average length of an edge was 2.7 ± 0.1 mm, and SvO₂ values were averaged along vessel segments of mean length 23.5 ± 2 mm. The resulting quantitative oxygenation

venograms that display absolute SvO₂ are shown in Figure 8. Mean SvO₂ across all graphed vein segments, was $62.5\% \pm 10\%$, $66.7\% \pm 7\%$, and $61.8\% \pm 10\%$, respectively, for each subject. SvO₂ for individual major cerebral vessels identified on the venograms ranged between 47.7% and 75.3% (Table 1). Significant SvO₂ differences were found between the individual veins ($P < 10^{-4}$, one-way analysis of variance across subjects). For instance, the superior anastomic vein was found to have higher SvO₂ relative to the straight or transverse sinuses, which may indicate the presence of residual partial-volume effects in the method.

Because the vessels were graphed from the volunteer QSM maps, it was also possible to probe SvO₂ across vessel tilt angle relative to B₀ in vivo. The vein tilt angle was determined for each vessel segment from the spatial coordinates of its two end nodes. The SvO₂ values measured in vivo for one volunteer are plotted versus tilt angle for all vessel edges in Figure 6c. SvO₂ values ranged between 64.3% and 69.1% over all vein tilt angles in this subject.

DISCUSSION

We have introduced a new method to reconstruct quantitative oxygenation venograms that display SvO₂ values along the venous vasculature of the human brain. The proposed method applies QSM analysis onto MRI phase images, which are sensitive to oxygenation-dependent variations of magnetic susceptibility in venous blood. For this study, we demonstrate feasibility of the technique in healthy subjects at 3T. Mean cerebral SvO₂ at baseline in these volunteers ranged from 61.8% to 66.7%, which is consistent with recent SvO₂ measurements of $61.0\% \pm 6\%$ and $57.0\% \pm 6\%$ by autoradiographic (57) and dynamic (58) and ¹⁵O positron emission tomography (PET) imaging, respectively.

Previous studies have used phase images to quantify SvO₂ through modeling brain vessels as long, parallel cylinders (10,14–17). While this susceptometry approach is relatively straightforward to implement, reliable SvO₂ estimation in practice depends on accurate knowledge of vessel tilt and manual identification of vessel segments for which the infinite cylinder model is appropriate. For these reasons, the set of brain vessels amenable to oxygen saturation measurements by means of MR susceptometry is limited. To achieve orientation-independent, 3D reconstruction of veins, Haacke et al instead applied inverse filter truncation to SWI phase images after high-pass filtering (59). This literature described the effect of vessel size on vein contrast in the susceptibility images and found physiological reasonable SvO₂ in vessels that were 8 mm or 16 mm in size. In contrast, our study proposes to reconstruct comprehensive oxygenation venograms through use of regularization with prior information imposed on the spatial gradients of χ .

One challenge with the proposed technique is selection of the regularization weighting parameter λ for accurate SvO₂ estimation. Under-regularized solutions may present increased noise level and streaking artifacts values near the air–tissue interfaces, while over-regularization may result in an overly smoothed susceptibility map that underestimates χ_{vein} , resulting in nearly 40% absolute error SvO₂ for large λ values. In practice, because the ground truth susceptibility distribution is unknown, selection of λ necessarily relies on heuristic approaches. Here the discrepancy principle was used to identify the optimal parameters of $\lambda_1 = 4.5 \cdot 10^{-4}$ and $\lambda_2 = 1.0 \cdot 10^{-2}$ for ℓ_1 - and ℓ_2 -regularized QSM in vivo.

These values are similar to $\lambda_1 = 2.0 \cdot 10^{-4}$ and $\lambda_2 = 1.5 \cdot 10^{-2}$ identified by means of a distinct heuristic known as the L-curve approach (60) in a separate study from our group (21).

In previous work with large anatomical structures such as the basal ganglia, the choice of ℓ_1 versus ℓ_2 norm did not heavily influence susceptibility values for iron quantification (21). However, we detected higher SvO₂ in vessels from ℓ_2 -regularized QSM relative to ℓ_1 -regularized QSM, both in numerical simulation and in vivo. This finding suggests that the smooth QSM solution promoted by ℓ_2 regularization is a suboptimal prior compared with the piecewise-constant solution promoted by ℓ_1 regularization for susceptibility quantification in narrow vascular structures. We also observed that ℓ_1 regularization provided less SvO₂ estimation variance for the majority of vessel tilt orientations in simulation compared with ℓ_2 regularization.

This study also compared SvO₂ values from the new QSM approach with traditional MR susceptometry methods in the literature. One drawback to homodyne filtering of phase images used in past studies is the effect of filter length on oxygenation values. Not surprisingly, we found that mean SvO₂ estimated from phase was statistically different for various Hanning filter lengths, which comports with previous work attributing up to 12% SvO₂ variation to filter size differences (61). In this work, background field was removed by means of the PDF algorithm, which is expected to provide more accurate, parameter-independent removal of global field compared with homodyne filtering. Model-based SvO₂ values from the resulting local field map were not statistically different from SvO₂ values directly calibrated from the QSM maps. These results suggest that the new QSM method is consistent with previous MR susceptometry approaches for oxygenation assessment in vessels parallel to B₀.

Furthermore, marked improvement in SvO₂ accuracy was achieved for veins that were not parallel to B₀ through use of QSM instead of MR susceptometry. One major benefit of vessel graphing in the study was the ability to probe SvO₂ values versus vessel tilt angle in vivo. Mean SvO₂ in vivo varied between 64.3% and 69.1% in vivo across all vessel tilt angles, which is consistent with less than 10% error over all vessel tilt angles expected from our numerical simulations with ℓ_1 -QSM. SvO₂ estimates from QSM are thus more robust across vessel orientation than MR susceptometry, which exhibits nearly 40% error for vessel tilt angles near the magic angle (20). As such, QSM enables oxygenation assessment over the full range of vessel tilt angles, which was previously unattainable by MR susceptometry.

Nonetheless, our numerical simulations suggest residual SvO₂ bias from QSM at some vessel tilt angles, with peak at 45° relative to B₀. This residual bias may occur for vessel orientations that contain considerable Fourier energy at the nulls and small values of the dipole kernel. In the future, we will explore the incorporation of priors based on vascular anatomy into the QSM reconstruction to reduce this observed bias. For this purpose, the proposed vessel graphing may provide valuable 3D vascular models directly from bright veins in the QSM maps. Our technique will benefit from improvements to graphing routines, such as preprocessing of MR data with contrast enhancement methods, which may also reduce the need for manual editing to achieve reliable venograms.

We note that in this work, hematocrit values were assumed to be uniformly $Hct = 0.40$ for each subject. Hematocrit is widely variable between individuals, and typical values range between 0.41 and 0.46 (62). For the in vivo susceptibility values estimated in this study, this variability corresponds to estimated mean SvO_2 range between 64.6% (for low hematocrit) and 68.4% (for high hematocrit) across the volunteers. Additionally, there is a considerable gender difference in Hct , with normal values ranging between 0.41 and 0.54 for males and between 0.37 and 0.47 for females (62). In future work, this parameter may be measured in each subject using a finger prick blood draw for more accurate oxygenation estimates.

Another limitation of the study is potential partial volume effects between narrow veins and the surrounding tissue, which may persist despite our use of the maximum value in each cylindrical vessel ROI to estimate χ_{vein} . Partial voluming can lead to underestimation of $\chi_{vein-water}$ from the QSM map, and thus overestimation in SvO_2 . This effect may explain why SvO_2 in the smaller superior anastomic vein tended to be higher than SvO_2 in larger draining veins such as the sagittal sinus (Table 1). Partial voluming may also explain much of the variation in SvO_2 at each tilt angle for the in vivo plot from Figure 6b. In future work, we propose use of vascular anatomical priors with more accurate estimates of vessel diameter to explicitly model and minimize partial volume effects.

The proposed method take advantage of higher SNR at ultra-high field such as 7T to achieve resolutions of 0.4 mm isotropic or smaller (44) for SvO_2 analysis in smaller cerebral veins that are more indicative of regional brain oxygen metabolism. Maximum intensity projections of QSM maps at 7T have been presented as a potential approach to visualize and probe blood oxygenation in small brain vessels (63). However, long acquisition times (~16 min) and QSM reconstruction times (~1 h per dataset) currently preclude efficient application of our method to large matrix sizes. Acquisition of larger datasets at 7T will require more efficient sampling to maintain high spatial resolution with shorter scan times (64). Similarly, fast reconstruction at the MRI scanner is necessary for clinical settings and can accelerated with use of graphical processing cards (65).

For the new technique to be clinically applicable, further work is necessary to assess the source of variability in tracked vessel locations and SvO_2 values between subjects. For instance, the venogram structures in Figure 8 varied between the three volunteers and it is unclear whether these differences are normal or can attributed to limitations in vessel tracking routines. To address this question, QSM venograms may be compared with standard venography MRI methods such as time-of-flight and phase-contrast scans in additional studies. Furthermore, spatial variations in SvO_2 were found across the venograms. This observation is not expected because previous PET studies revealed fairly uniform oxygenation levels across the brain (66). Nonphysiological sources of this variability may include imperfect vessel tracking, suboptimal extraction of χ_{vein} values, partial volume effects, and residual angle-dependent bias in SvO_2 and should be addressed in future work.

We have proposed a novel method for quantitative oxygenation venography from QSM. Our study presented physiologically meaningful SvO_2 values for individual vessels, including large draining veins such as the superior sagittal and transverse sinuses; as well as smaller pial veins such as the superior anastomic vein. The MRI acquisition for the new method is

related to SWI scans which have already found use in the clinic (67–69). In addition to SWI magnitude contrast for veins, our method can provide baseline SvO₂ values along the venous vasculature from the same dataset. If current limitations with the method are successfully overcome, quantitative oxygenation venograms may have direct impact in clinical management of disease such as acute stroke and brain tumor; and may provide earlier biomarkers for diagnosis of neurodegenerative disorders such as MS, Alzheimer's and Huntington's Diseases.

Acknowledgments

Grant sponsor: National Science Foundation Graduate Research Fellowship, the Advanced Multimodal Neuroimaging Training Program; Grant number: R90-DA023427; Grant sponsor: National Institutes of Health; Grant number: R01-EB007942.

References

- Ito H, Ibaraki M, Kanno I, Fukuda H, Miura S. Changes in cerebral blood flow and cerebral oxygen metabolism during neural activation measured by positron emission tomography: comparison with blood oxygenation level-dependent contrast measured by functional magnetic resonance imaging. *J Cereb Blood Flow Metab.* 2005; 25:371–377. [PubMed: 15660103]
- Davis TL, Kwong KK, Weisskoff RM, Rosen BR. Calibrated functional MRI: mapping the dynamics of oxidative metabolism. *Proc Natl Acad Sci U S A.* 1998; 95:1834–1839. [PubMed: 9465103]
- Baron JC, Boussier MG, Rey A, Guillard A, Comar D, Castaigne P. Reversal of focal “miserere-perfusion syndrome” by extra-intracranial arterial bypass in hemodynamic cerebral ischemia. A case study with 15O positron emission tomography. *Stroke.* 1981; 12:454–459. [PubMed: 6976022]
- Sobesky J, Zaro Weber O, Lehnhardt FG, Hesselmann V, Neveling M, Jacobs A, Heiss WD. Does the mismatch match the penumbra? Magnetic resonance imaging and positron emission tomography in early ischemic stroke. *Stroke.* 2005; 36:980–985. [PubMed: 15790950]
- Heiss WD, Kracht L, Grond M, Rudolf J, Bauer B, Wienhard K, Pawlik G. Early [(11)C]Flumazenil/H(2)O positron emission tomography predicts irreversible ischemic cortical damage in stroke patients receiving acute thrombolytic therapy. *Stroke.* 2000; 31:366–369. [PubMed: 10657407]
- Nordmark M, Bentzen SM, Rudat V, et al. Prognostic value of tumor oxygenation in 397 head and neck tumors after primary radiation therapy. An international multi-center study. *Radiother Oncol.* 2005; 77:18–24. [PubMed: 16098619]
- Leenders KL, Beaney RP, Brooks DJ, Lammertsma AA, Heather JD, McKenzie CG. Dexamethasone treatment of brain tumor patients: effects on regional cerebral blood flow, blood volume, and oxygen utilization. *Neurology.* 1985; 35:1610–1616. [PubMed: 4058751]
- Fan, AP.; Kinkel, RP.; Madigan, NK.; Nielsen, AS.; Benner, T.; Tinelli, E.; Rosen, BR.; Adalsteinsson, E.; Mainero, C. Cortical oxygen extraction as a marker of disease stage and function in multiple sclerosis: a quantitative study using 7 Tesla MRI susceptibility. Proceedings of the 20th Annual Meeting of ISMRM; Melbourne, Australia. 2012. p. Abstract 498
- Ge Y, Zhang Z, Lu H, Tang L, Jaggi H, Herbert J, Babb JS, Rusinek H, Grossman RI. Characterizing brain oxygen metabolism in patients with multiple sclerosis with T2-relaxation-under-spin-tagging MRI. *J Cereb Blood Flow Metab.* 2012; 32:403–412. [PubMed: 22252237]
- Weisskoff RM, Kiihne S. MRI susceptometry: image-based measurement of absolute susceptibility of MR contrast agents and human blood. *Magn Reson Med.* 1992; 24:375–383. [PubMed: 1569876]
- Sedlacik J, Rauscher A, Reichenbach JR. Obtaining blood oxygenation levels from MR signal behavior in the presence of single venous vessels. *Magn Reson Med.* 2007; 58:1035–1044. [PubMed: 17969121]

12. Sedlacik J, Rauscher A, Reichenbach JR. Quantification of modulated blood oxygenation levels in single cerebral veins by investigating their MR signal decay. *Z Med Phys.* 2009; 19:48–57. [PubMed: 19459585]
13. Dagher J, Du YP. Efficient and robust estimation of blood oxygenation levels in single cerebral veins. *Med Biol Eng Comput.* 2012; 50:473–482. [PubMed: 22415740]
14. Fernandez-Seara MA, Techawiboonwong A, Detre JA, Wehrli FW. MR susceptometry for measuring global brain oxygen extraction. *Magn Reson Med.* 2006; 55:967–973. [PubMed: 16598726]
15. Jain V, Langham MC, Wehrli FW. MRI estimation of global brain oxygen consumption rate. *J Cereb Blood Flow Metab.* 2010; 30:1598–1607. [PubMed: 20407465]
16. Fan AP, Benner T, Bolar DS, Rosen BR, Adalsteinsson E. Phase-based regional oxygen metabolism (PROM) using MRI. *Magn Reson Med.* 2012; 67:669–678. [PubMed: 21713981]
17. Haacke EM, Lai S, Reichenbach JR, Kuppusamy K, Hoogenraad FG, Takeichi H, Lin W. In vivo measurement of blood oxygen saturation using magnetic resonance imaging: a direct validation of the blood oxygen level-dependent concept in functional brain imaging. *Hum Brain Mapp.* 1997; 5:341–346. [PubMed: 20408238]
18. Jain V, Langham MC, Floyd TF, Jain G, Magland JF, Wehrli FW. Rapid magnetic resonance measurement of global cerebral metabolic rate of oxygen consumption in humans during rest and hypercapnia. *J Cereb Blood Flow Metab.* 2011; 31:1504–1512. [PubMed: 21505481]
19. Langham MC, Magland JF, Epstein CL, Floyd TF, Wehrli FW. Accuracy and precision of MR blood oximetry based on the long paramagnetic cylinder approximation of large vessels. *Magn Reson Med.* 2009; 62:333–340. [PubMed: 19526517]
20. Li C, Langham MC, Epstein CL, Magland JF, Wu J, Gee J, Wehrli FW. Accuracy of the cylinder approximation for susceptometric measurement of intravascular oxygen saturation. *Magn Reson Med.* 2012; 67:808–813. [PubMed: 21858859]
21. Bilgic B, Pfefferbaum A, Rohlfing T, Sullivan EV, Adalsteinsson E. MRI estimates of brain iron concentration in normal aging using quantitative susceptibility mapping. *Neuroimage.* 2012; 59:2625–2635. [PubMed: 21925274]
22. Schweser F, Deistung A, Lehr BW, Reichenbach JR. Quantitative imaging of intrinsic magnetic tissue properties using MRI signal phase: an approach to in vivo brain iron metabolism? *Neuroimage.* 2011; 54:2789–2807. [PubMed: 21040794]
23. Liu C, Li W, Wu B, Jiang Y, Johnson GA. 3D fiber tractography with susceptibility tensor imaging. *Neuroimage.* 2012; 59:1290–1298. [PubMed: 21867759]
24. Schweser F, Deistung A, Lehr BW, Reichenbach JR. Differentiation between diamagnetic and paramagnetic cerebral lesions based on magnetic susceptibility mapping. *Med Phys.* 2010; 37:5165–5178. [PubMed: 21089750]
25. Liu T, Surapaneni K, Lou M, Cheng L, Spincemaille P, Wang Y. Cerebral microbleeds: burden assessment by using quantitative susceptibility mapping. *Radiology.* 2012; 262:269–278. [PubMed: 22056688]
26. Marques JP, Bowtell R. Application of a fourier-based method for rapid calculation of field inhomogeneity due to spatial variation of magnetic susceptibility. *Concepts Magn Reson Part B Magn Reson Eng.* 2005; 25B:65–78.
27. Salomir R, De Senneville BD, Moonen CTW. A fast calculation method for magnetic field inhomogeneity due to an arbitrary distribution of bulk susceptibility. *Concepts Magn Reson Part B Magn Reson Eng.* 2003; 19B:26–34.
28. Wharton S, Schafer A, Bowtell R. Susceptibility mapping in the human brain using threshold-based k-space division. *Magn Reson Med.* 2010; 63:1292–1304. [PubMed: 20432300]
29. Shmueli K, de Zwart JA, van Gelderen P, Li TQ, Dodd SJ, Duyn JH. Magnetic susceptibility mapping of brain tissue in vivo using MRI phase data. *Magn Reson Med.* 2009; 62:1510–1522. [PubMed: 19859937]
30. Liu T, Spincemaille P, de Rochefort L, Kressler B, Wang Y. Calculation of Susceptibility Through Multiple Orientation Sampling (COSMOS): a method for conditioning the inverse problem from measured magnetic field map to susceptibility source image in MRI. *Magn Reson Med.* 2009; 61:196–204. [PubMed: 19097205]

31. Schweser F, Sommer K, Deistung A, Reichenbach JR. Quantitative susceptibility mapping for investigating subtle susceptibility variations in the human brain. *Neuroimage*. 2012; 62:2083–2100. [PubMed: 22659482]
32. Liu J, Liu T, de Rochefort L, et al. Morphology enabled dipole inversion for quantitative susceptibility mapping using structural consistency between the magnitude image and the susceptibility map. *Neuroimage*. 2012; 59:2560–2568. [PubMed: 21925276]
33. de Rochefort L, Liu T, Kressler B, Liu J, Spincemaille P, Lebon V, Wu JL, Wang Y. Quantitative susceptibility map reconstruction from MR phase data using bayesian regularization: validation and application to brain imaging. *Magn Reson Med*. 2010; 63:194–206. [PubMed: 19953507]
34. Liu T, Liu J, de Rochefort L, Spincemaille P, Khalidov I, Ledoux JR, Wang Y. Morphology Enabled Dipole Inversion (MEDI) from a singleangle acquisition: comparison with COSMOS in human brain imaging. *Magn Reson Med*. 2011; 66:777–783. [PubMed: 21465541]
35. Tsai PS, Kaufhold JP, Blinder P, Friedman B, Drew PJ, Karten HJ, Lyden PD, Kleinfeld D. Correlations of neuronal and microvascular densities in murine cortex revealed by direct counting and colocalization of nuclei and vessels. *J Neurosci*. 2009; 29:14553–14570. [PubMed: 19923289]
36. Spees WM, Yablonskiy DA, Oswood MC, Ackerman JJH. Water proton MR properties of human blood at 1.5 Tesla: magnetic susceptibility, T-1, T-2, T-2* and non-Lorentzian signal behavior. *Magn Reson Med*. 2001; 45:533–542. [PubMed: 11283978]
37. Jain V, Abdulmalik O, Propert KJ, Wehrli FW. Investigating the magnetic susceptibility properties of fresh human blood for noninvasive oxygen saturation quantification. *Magn Reson Med*. 2012; 68:863–867. [PubMed: 22162033]
38. Thulborn KR, Waterton JC, Matthews PM, Radda GK. Oxygenation dependence of the transverse relaxation time of water protons in whole blood at high field. *Biochim Biophys Acta*. 1982; 714:265–270. [PubMed: 6275909]
39. Plyavin YA, Blum EY. Magnetic parameters of blood cells and highgradient paramagnetic and diamagnetic phoresis. *Magneto hydrodynamics*. 1983; 19:349–359.
40. Guyton, AC.; Hall, JE. *Red blood cells, anemia, and polycythemia*. Philadelphia: Saunders; 2000.
41. Duyn JH, van Gelderen P, Li TQ, de Zwart JA, Koretsky AP, Fukunaga M. High-field MRI of brain cortical substructure based on signal phase. *Proc Natl Acad Sci U S A*. 2007; 104:11796–11801. [PubMed: 17586684]
42. Li W, Wu B, Liu C. Quantitative susceptibility mapping of human brain reflects spatial variation in tissue composition. *Neuroimage*. 2011; 55:1645–1656. [PubMed: 21224002]
43. Yao B, Li TQ, van Gelderen P, Shmueli K, de Zwart JA, Duyn JH. Susceptibility contrast in high field MRI of human brain as a function of tissue iron content. *Neuroimage*. 2009; 44:1259–1266. [PubMed: 19027861]
44. Deistung A, Schafer A, Schweser F, Biedermann U, Turner R, Reichenbach JR. Toward in vivo histology: a comparison of quantitative susceptibility mapping (QSM) with magnitude-, phase-, and R2*-imaging at ultra-high magnetic field strength. *Neuroimage*. 2013; 65:299–314. [PubMed: 23036448]
45. Kressler B, de Rochefort L, Liu T, Spincemaille P, Jiang Q, Wang Y. Nonlinear regularization for per voxel estimation of magnetic susceptibility distributions from MRI field maps. *IEEE Trans Med Imaging*. 2010; 29:273–281. [PubMed: 19502123]
46. Rohlfing T, Zahr NM, Sullivan EV, Pfefferbaum A. The SRI24 multichannel atlas of normal adult human brain structure. *Hum Brain Mapp*. 2010; 31:798–819. [PubMed: 20017133]
47. Hansen, PC. *Rank-deficient and discrete ill-posed problems: numerical aspects of linear inversion*. Philadelphia: SIAM; 1998.
48. Deistung A, Dittrich E, Sedlacik J, Rauscher A, Reichenbach JR. ToFSWI: simultaneous time of flight and fully flow compensated susceptibility weighted imaging. *J Magn Reson Imaging*. 2009; 29:1478–1484. [PubMed: 19472425]
49. Robinson S, Grabner G, Witoszynskij S, Trattnig S. Combining phase images from multi-channel RF coils using 3D phase offset maps derived from a dual-echo scan. *Magn Reson Med*. 2011; 65:1638–1648. [PubMed: 21254207]
50. Hammond KE, Lupo JM, Xu D, Metcalf M, Kelley DA, Pelletier D, Chang SM, Mukherjee P, Vigneron DB, Nelson SJ. Development of a robust method for generating 7.0 T multichannel

- phase images of the brain with application to normal volunteers and patients with neurological diseases. *Neuroimage*. 2008; 39:1682–1692. [PubMed: 18096412]
51. Jenkinson M. Fast, automated, N-dimensional phase-unwrapping algorithm. *Magn Reson Med*. 2003; 49:193–197. [PubMed: 12509838]
 52. Smith SM. Fast robust automated brain extraction. *Hum Brain Mapp*. 2002; 17:143–155. [PubMed: 12391568]
 53. Liu T, Khalidov I, de Rochefort L, Spincemaille P, Liu J, Tsiouris AJ, Wang Y. A novel background field removal method for MRI using projection onto dipole fields (PDF). *NMR Biomed*. 2011; 24:1129–1136. [PubMed: 21387445]
 54. Fang Q, Sakadzic S, Ruvinskaya L, Devor A, Dale AM, Boas DA. Oxygen advection and diffusion in a three-dimensional vascular anatomical network. *Opt Express*. 2008; 16:17530–17541. [PubMed: 18958033]
 55. Fang, QQ.; Boas, DA. Tetrahedral mesh generation from volumetric binary and gray-scale images. *Proceedings of the 6th IEEE International Symposium on Biomedical Imaging: From Nano to Macro*; Piscataway, NJ: IEEE Press; 2009. p. 1142–1145.
 56. Wang Y, Yu Y, Li D, Bae KT, Brown JJ, Lin W, Haacke EM. Artery and vein separation using susceptibility-dependent phase in contrast-enhanced MRA. *J Magn Reson Imaging*. 2000; 12:661–670. [PubMed: 11050635]
 57. Hattori N, Bergsneider M, Wu HM, Glenn TC, Vespa PM, Hovda DA, Phelps ME, Huang SC. Accuracy of a method using short inhalation of O-15-O-2 for measuring cerebral oxygen extraction fraction with PET in healthy humans. *J Nucl Med*. 2004; 45:765–770. [PubMed: 15136624]
 58. Bremner JP, van Berckel BN, Persoon S, Kappelle LJ, Lammertsma AA, Kloet R, Luurtsema G, Rijbroek A, Klijn CJ, Boellaard R. Day-to-day test-retest variability of CBF, CMRO2, and OEF measurements using dynamic 15O PET studies. *Mol Imaging Biol*. 2011; 13:759–768. [PubMed: 20700768]
 59. Haacke EM, Tang J, Neelavalli J, Cheng YC. Susceptibility mapping as a means to visualize veins and quantify oxygen saturation. *J Magn Reson Imaging*. 2010; 32:663–676. [PubMed: 20815065]
 60. Hansen PC. The L-curve and its use in the numerical treatment of inverse problems. *Comput Inverse Probl Electrodynam*. 2000:119–142.
 61. Langham MC, Magland JF, Floyd TF, Wehrli FW. Retrospective correction for induced magnetic field inhomogeneity in measurements of large-vessel hemoglobin oxygen saturation by MR susceptometry. *Magn Reson Med*. 2009; 61:626–633. [PubMed: 19107914]
 62. Reichenbach JR, Haacke EM. High-resolution BOLD venographic imaging: a window into brain function. *NMR Biomed*. 2001; 14:453–467. [PubMed: 11746938]
 63. Christen T, Bolar DS, Zaharchuk G. Imaging brain oxygenation with MRI using blood oxygenation approaches: methods, validation, and clinical applications. *AJNR Am J Neuroradiol*. 2013; 34:1113–1123. [PubMed: 22859287]
 64. Wu B, Li W, Guidon A, Liu C. Whole brain susceptibility mapping using compressed sensing. *Magn Reson Med*. 2012; 67:137–147. [PubMed: 21671269]
 65. Abuhashem, OA.; Bilgic, B.; Adalsteinsson, E. GPU Accelerated quantitative susceptibility mapping. *Proceedings of the 20th Annual Meeting of ISMRM*; Melbourne, Australia. 2012. p. Abstract 3442
 66. Ishii K, Sasaki M, Kitagaki H, Sakamoto S, Yamaji S, Maeda K. Regional difference in cerebral blood flow and oxidative metabolism in human cortex. *J Nucl Med*. 1996; 37:1086–1088. [PubMed: 8965174]
 67. Sehgal V, Delproposto Z, Haacke EM, Tong KA, Wycliffe N, Kido DK, Xu Y, Neelavalli J, Haddar D, Reichenbach JR. Clinical applications of neuroimaging with susceptibility-weighted imaging. *J Magn Reson Imaging*. 2005; 22:439–450. [PubMed: 16163700]
 68. Idhahbi A, Boukobza M, Crassard I, Porcher R, Bousser MG, Chabriat H. MRI of clot in cerebral venous thrombosis: high diagnostic value of susceptibility-weighted images. *Stroke*. 2006; 37:991–995. [PubMed: 16484607]
 69. Hammond, KE.; Lupo, JM.; Xu, D.; Veeraraghavan, S.; Lee, H.; Kincaid, A.; Vigneron, DB.; Manley, GT.; Nelson, SJ.; Mukherjee, P. Microbleed detection in traumatic brain injury at 3T and

7T: comparing 2D and 3D Gradient-Recalled Echo (GRE) imaging with Susceptibility-Weighted Imaging (SWI). Proceedings of the 18th Annual Meeting of ISMRM; Honolulu, Hawaii. 2009. p. Abstract 248

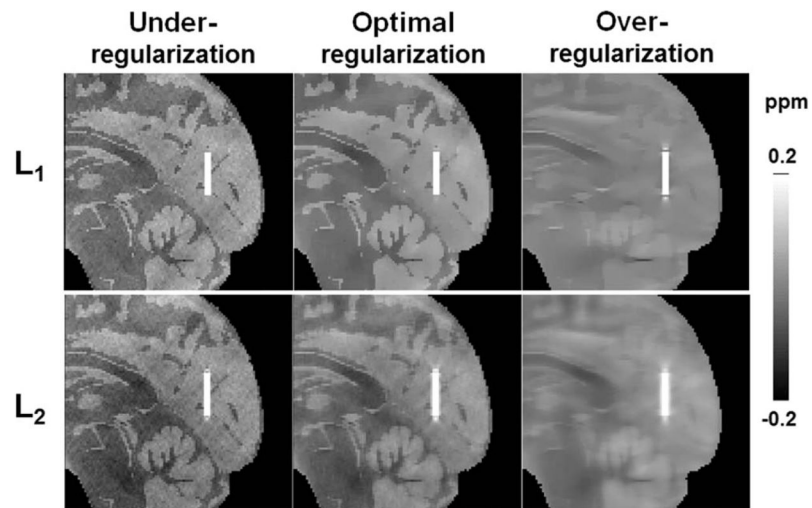


FIG. 1.

Susceptibility mapping results with ℓ_1 and ℓ_2 regularization in numerical simulation of a parallel vessel. The optimal regularization weighting parameters determined by the discrepancy principle were $\lambda_1 = 3.0 \cdot 10^{-4}$ and $\lambda_2 = 1.5 \cdot 10^{-2}$. Images are also shown for under-regularized solutions with smaller regularization weighting than optimum ($\lambda_1 = 5.0 \cdot 10^{-5}$ and $\lambda_2 = 2.0 \cdot 10^{-3}$); as well as over-regularized solutions with larger regularization weighting than optimum ($\lambda_1 = 3.0 \cdot 10^{-3}$ and $\lambda_2 = 0.2$).

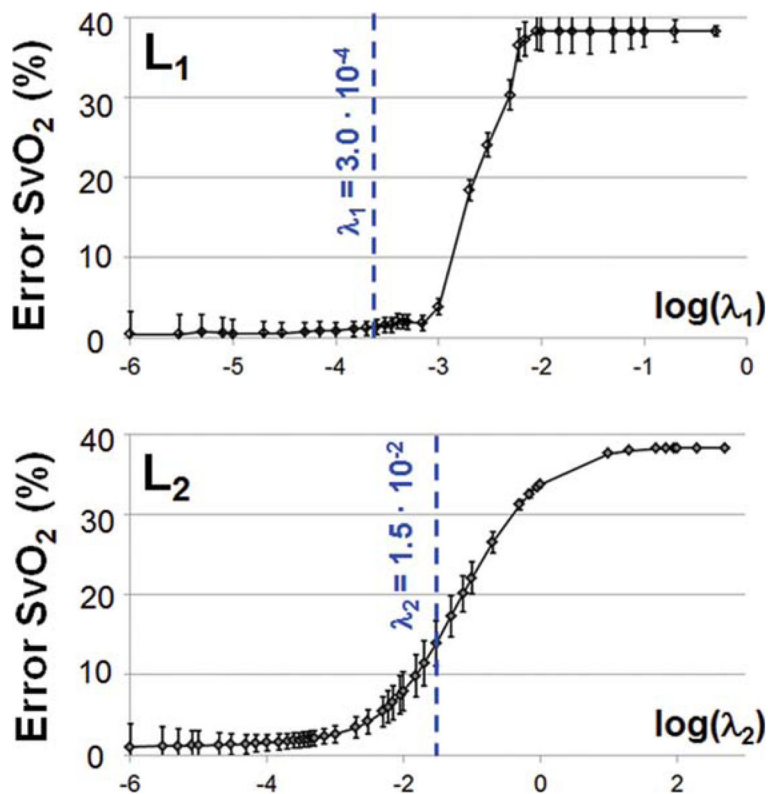
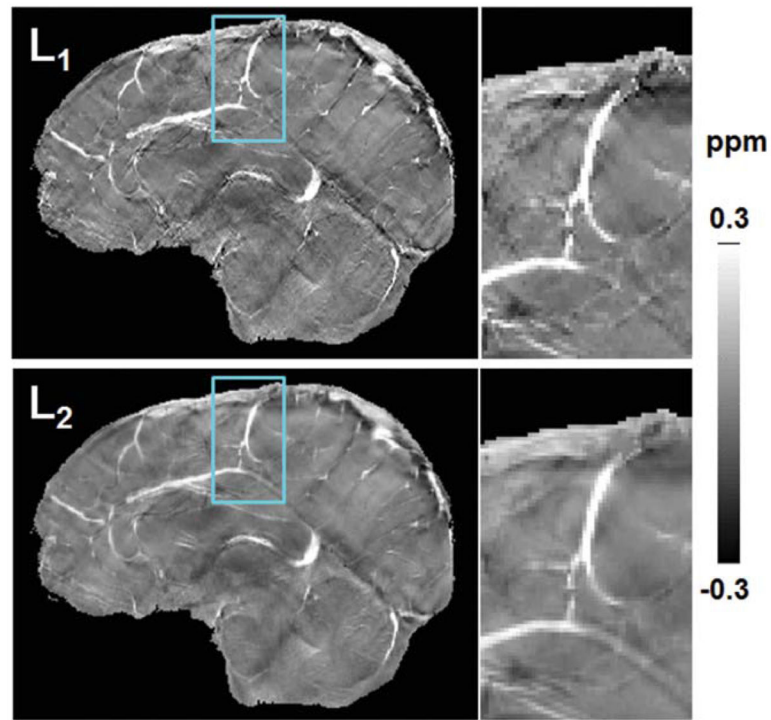


FIG. 2.

Plot of absolute SvO₂ error in venous oxygenation (%) from QSM across regularization weighting parameters in numerical simulation. At the optimal weighting of $\lambda_1 = 3.0 \cdot 10^{-4}$, ℓ_1 -regularized QSM resulted in 1.6% error. In contrast, at the optimal weighting of $\lambda_2 = 1.5 \cdot 10^{-2}$, ℓ_2 -regularized QSM resulted in 6.9% error. [[Color figure can be viewed in the online issue, which is available at wileyonlinelibrary.com.]]

**FIG. 3.**

The same sagittal slice is shown for in vivo susceptibility maps from ℓ_1 - and ℓ_2 -regularized QSM. The susceptibility maps were created at the optimal regularization parameters for the in vivo data, $\lambda_1 = 4.5 \cdot 10^{-4}$ and $\lambda_2 = 1.0 \cdot 10^{-2}$. The zoomed inset highlights a cortical pial vessel on the susceptibility maps. SvO_2 from QSM in this cortical vein was 66.5% and 70.3% for ℓ_1 and ℓ_2 regularization, respectively. [Color figure can be viewed in the online issue, which is available at wileyonlinelibrary.com.]

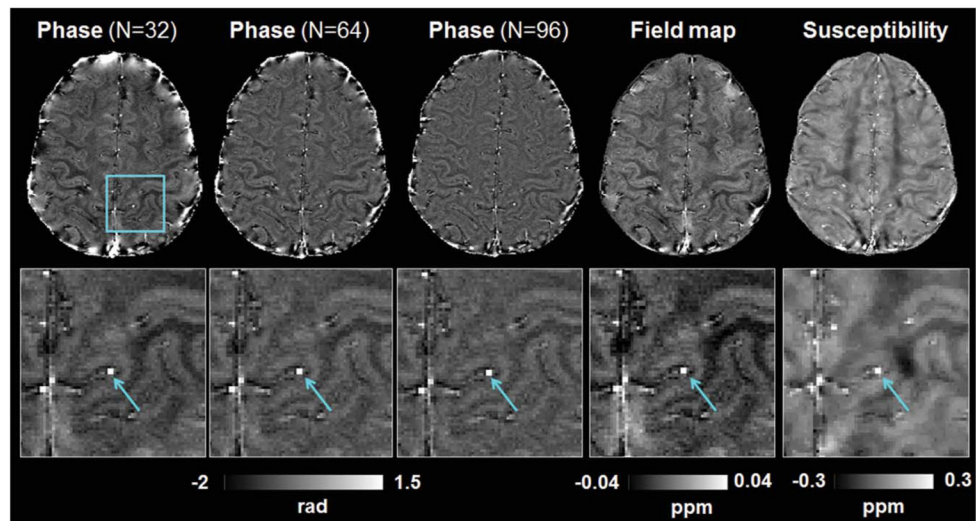


FIG. 4. Parallel vessel identified on the same slice in phase, field map, and susceptibility images. The phase images at TE = 20.3ms are shown after removal of background signal and phase wraps with Hanning filter of width 96/512, 64/512, and 32/512 of the image matrix size respectively. The field map image is shown after removal of undesired global fields estimated by projection onto dipole fields (53). The susceptibility map was reconstructed with ℓ_1 regularization at the optimal weighting of $\lambda_1 = 4.5 \cdot 10^{-4}$. The same cross-section of the parallel vessel is shown in all insets (blue arrows). [Color figure can be viewed in the online issue, which is available at wileyonlinelibrary.com.]

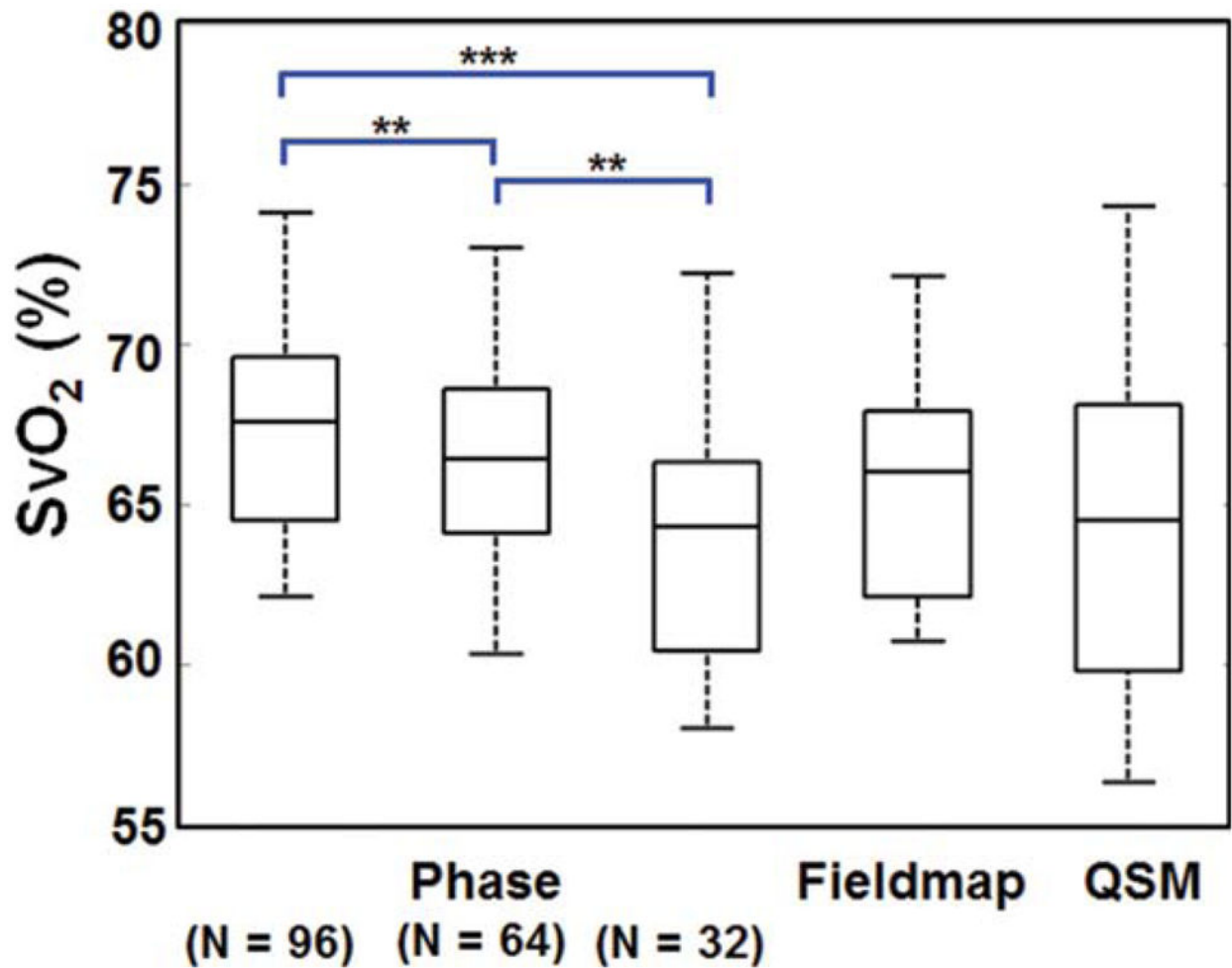


FIG. 5.

Comparison of SvO₂ from MR susceptibility with SvO₂ from QSM in 10 parallel vessels from one volunteer. SvO₂ values from phase and field map images are made using MR susceptibility, in which vessels are modeled as long cylinders. In contrast, SvO₂ from QSM is directly quantified from susceptibility values recovered in the vessels. Mean SvO₂ values from phase images corresponding to different filter widths are statistically different after Bonferroni correction. (** indicates P value $< 10^{-2}$ and *** indicates P value $< 10^{-3}$). However, there is no detectable difference between mean SvO₂ from QSM and mean SvO₂ from MR susceptibility applied on the field map. [Color figure can be viewed in the online issue, which is available at wileyonlinelibrary.com.]

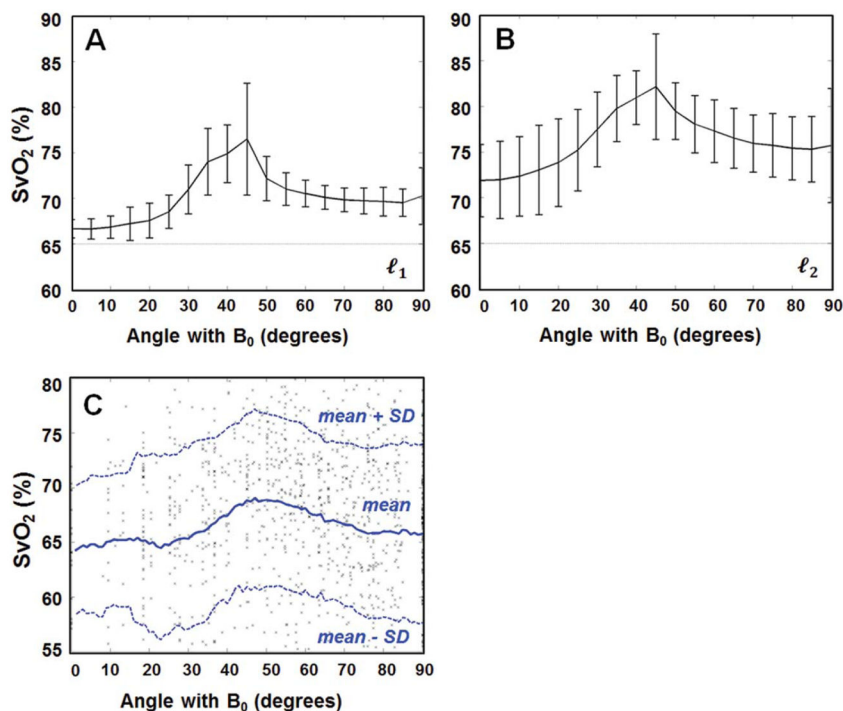


FIG. 6. Mean SvO₂ from QSM in numerical simulation across vessel tilt angle with respect to the main field (B₀) for (A) ℓ_1 -regularized and (B) ℓ_2 -regularized QSM algorithms. The error bars indicate standard deviation of estimated SvO₂ and the dotted line delineates the true simulated value of 65% (dotted line). **C:** Mean SvO₂ from QSM across vessel tilt angle observed in vivo from one healthy volunteer. Each data point represents a SvO₂ measurement from a single vessel edge. [Color figure can be viewed in the online issue, which is available at wileyonlinelibrary.com.]

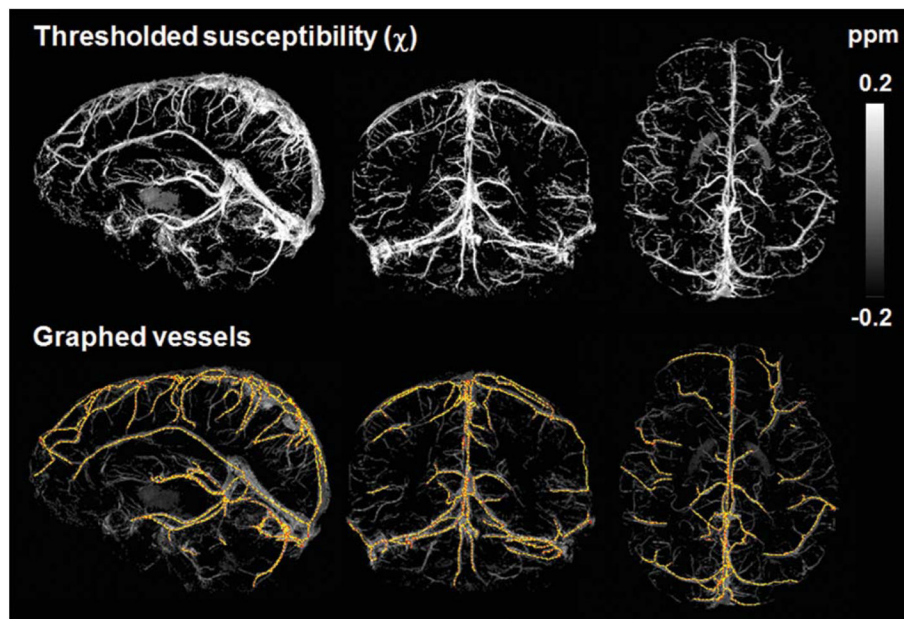


FIG. 7. Susceptibility map in one healthy volunteer thresholded at $\chi > 0.15$, and the corresponding vessels that are graphed by the Volumetric Image Data Analysis software in MATLAB (35). In this volunteer, the venous vasculature is represented by a total of 1090 edges inside the vessels. [Color figure can be viewed in the online issue, which is available at wileyonlinelibrary.com.]

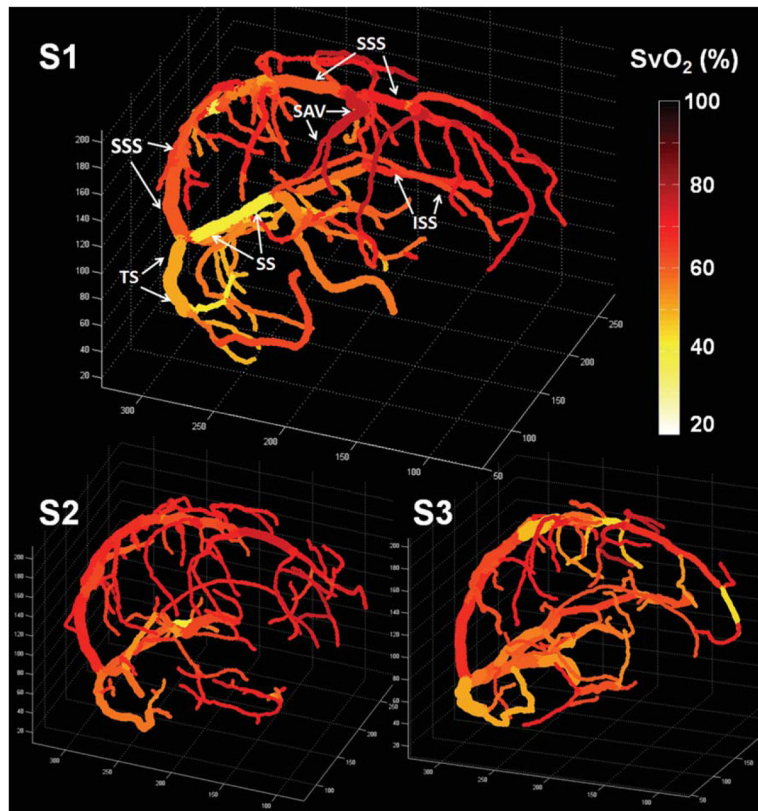


FIG. 8. Quantitative oxygenation venograms that display baseline SvO_2 along each vein in three healthy volunteers. In the first subject, major veins in the brain are labeled, including the superior sagittal sinus (SSS), inferior sagittal sinus (ISS), straight sinus (SS), transverse sinus (TS), and superior anastomotic vein (SAV).

Table 1Mean Absolute SvO₂ (%) Levels in Major Veins of the Brain for Three Healthy Volunteers

Vein	Subject 1	Subject 2	Subject 3	Mean across subjects
Superior sagittal sinus (SSS)	61.8 ± 9	67.6 ± 6	62.0 ± 10	63.8 ± 3
Inferior sagittal sinus (ISS)	62.7 ± 10	67.6 ± 10	62.0 ± 12	64.1 ± 3
Straight sinus (SS)	47.7 ± 11	53.4 ± 4	56.2 ± 3	52.4 ± 4
Transverse sinus (right) (TS-R)	56.6 ± 6	60.0 ± 6	58.6 ± 8	58.4 ± 2
Transverse sinus (left) (TS-L)	51.7 ± 6	57.5 ± 6	50.7 ± 10	53.3 ± 4
Superior anastomic vein (SAV)	75.3 ± 4	70.2 ± 5	71.0 ± 7	72.2 ± 3